Real-Space Imaging of Kondo Screening in a Two-Dimensional O_2 Lattice

Ying Jiang, *et al.*

Science **333**, 324 (2011);
DOI: 10.1126/science.1205785

$\varepsilon > 0$. Their value $\gamma = 0.055\ldots$ for the critical exponent is extremely small, explaining why finite-sized simulations seem to suggest a discontinuity. Our argument gives (for any rule) a rigorous upper bound on $\rho(t_c + \varepsilon)$ that tends to 0 as $\varepsilon \to 0$, but only in a (doubly) logarithmic fashion.

Given the track record of simulations for these models, a very interesting open question is whether these power-law predictions can be established rigorously, and for which rules. Here the powder-keg viewpoint may help. The simulation results in Fig. 2 (for PR) show that initially a powder keg does develop, but as the transition is approached from below, it spreads out and flattens. A precise analysis of this spreading may perhaps lead to a rigorous understanding of the details of the phase transition.

Mathematically, further intriguing and basic questions remain open. We call a random graph process locally convergent if for each fixed k there is a function $\rho_k(t)$ such that when $m \sim tn$ the (random) number of vertices in components of size k is with high probability close to $\rho_k(t)n$ when n is large. Similarly, it is globally convergent if there is a function $\rho(t)$ such that the size of the largest component after tn steps is concentrated around $\rho(t)n$; i.e., if the scaling limit exists. Such convergence is often assumed without comment but should not be taken for granted. For example, in the Barabási-Albert network model, early random variations when the degrees are small may be frozen-in by the preferential attachment, and the rescaled maximum degree converges to a probability distribution, not to a single value (*27*). Something similar could in principle occur in Achlioptas processes. Our argument can also be written to avoid assuming convergence (*17*).

The Achlioptas processes that have been studied in the mathematics literature (*28*–*32*) almost always use rules from a restricted class (bounded-size rules) known to be locally convergent and conjectured to be globally convergent (*30*); rules outside this class are often regarded as intractable. A simple modification of our argument shows that all locally convergent Achlioptas processes are globally convergent, settling this conjecture. A very intriguing open question is whether the product rule (which is not bounded-size) is convergent.

Finally, it is clear that if one departs far enough from the ER model, then a discontinuous transition is possible. For example, suppose that at every step the two smallest components in the whole graph are joined. With n a power of 2, this corresponds to filling in the edges of a binary tree from the leaves to the root, so the largest component grows extremely quickly in the last few steps (*16*). Our argument shows [see (*15*)] that any rule based on picking a fixed number of random vertices gives a continuous transition; considering all n vertices can give a discontinuous one. Where is the cutoff? It turns out that it is at the lower end of the range: Whenever $l \to \infty$ as $n \to \infty$, then the rule "pick l vertices at random and join the two smallest distinct components selected" exhibits explosive percolation (*15*).

References and Notes

1. P. Erdős, A. Rényi, *Publ. Math. Inst. Hungar. Acad. Sci.* **5**, 17 (1960).
2. B. Bollobás, *Trans. Am. Math. Soc.* **286**, 257 (1984).
3. T. Łuczak, *Random Struct. Algorithms* **1**, 287 (1990).
4. S. Janson, D. E. Knuth, T. Łuczak, B. Pittel, *Random Struct. Algorithms* **4**, 233 (1993).
5. B. Pittel, N. C. Wormald, *J. Comb. Theory Ser. B* **93**, 127 (2005).
6. A.-L. Barabási, R. Albert, *Science* **286**, 509 (1999).
7. R. Albert, H. Jeong, A.-L. Barabási, *Nature* **406**, 378 (2000).
8. B. Bollobás, O. Riordan, *Internet Math.* **1**, 1 (2003).
9. R. Pastor-Satorras, A. Vespignani, *Phys. Rev. Lett.* **86**, 3200 (2001).
10. A. L. Lloyd, R. M. May, *Science* **292**, 1316 (2001).
11. B. Bollobás, S. Janson, O. Riordan, *Random Struct. Algorithms* **31**, 3 (2007).
12. O. Riordan, *Combin. Probab. Comput.* **14**, 897 (2005).
13. D. Achlioptas, R. M. D'Souza, J. Spencer, *Science* **323**, 1453 (2009).
14. Y. Azar, A. Z. Broder, A. R. Karlin, E. Upfal, *SIAM J. Comput.* **29**, 180 (1999).
15. See the supporting online material on *Science* Online.
16. E. J. Friedman, A. S. Landsberg, *Phys. Rev. Lett.* **103**, 255701 (2009).
17. O. Riordan, L. Warnke, preprint available at http://arxiv.org/abs/1102.5306 (2011).
18. T. Bohman, *Science* **323**, 1438 (2009).
19. Y. S. Cho, J. S. Kim, J. Park, B. Kahng, D. Kim, *Phys. Rev. Lett.* **103**, 135702 (2009).
20. F. Radicchi, S. Fortunato, *Phys. Rev. Lett.* **103**, 168701 (2009).
21. F. Radicchi, S. Fortunato, *Phys. Rev. E Stat. Nonlin. Soft Matter Phys.* **81**, 036110 (2010).
22. Y. S. Cho, S.-W. Kim, J. D. Noh, B. Kahng, D. Kim, *Phys. Rev. E Stat. Nonlin. Soft Matter Phys.* **82**, 042102 (2010).
23. R. M. D'Souza, M. Mitzenmacher, *Phys. Rev. Lett.* **104**, 195702 (2010).
24. R. M. Ziff, *Phys. Rev. E Stat. Nonlin. Soft Matter Phys.* **82**, 051105 (2010).
25. J. Nagler, A. Levina, M. Timme, *Nat. Phys.* **7**, 265 (2011).
26. R. A. da Costa, S. N. Dorogovtsev, A. V. Goltsev, J. F. F. Mendes, *Phys. Rev. Lett.* **105**, 255701 (2010).
27. B. Bollobás, O. Riordan, *Handbook of Graphs and Networks* (Wiley, Weinheim, Germany, 2003), pp. 1–34.
28. T. Bohman, A. Frieze, *Random Struct. Algorithms* **19**, 75 (2001).
29. T. Bohman, D. Kravitz, *Combin. Probab. Comput.* **15**, 489 (2006).
30. J. Spencer, N. C. Wormald, *Combinatorica* **27**, 587 (2007).
31. A. Beveridge, T. Bohman, A. Frieze, O. Pikhurko, *SIAM J. Discrete Math.* **23**, 993 (2009).
32. S. Janson, J. Spencer, preprint available at http://arxiv.org/abs/1005.4494 (2010).

Acknowledgments: L.W.'s research was supported by an Engineering and Physical Sciences Research Council Research Studentship and a Scatcherd European Scholarship.

Supporting Online Material

www.sciencemag.org/cgi/content/full/333/6040/322/DC1
SOM Text
References (*33*–*35*)

28 March 2011; accepted 17 May 2011
10.1126/science.1206241

Real-Space Imaging of Kondo Screening in a Two-Dimensional O_2 Lattice

Ying Jiang,[1,2] Y. N. Zhang,[1] J. X. Cao,[1,3] R. Q. Wu,[1] W. Ho[1,4]*

Kondo lattice systems can exhibit unusual many-body behaviors that result from the interplay between onsite Kondo screening and intersite coupling. We used scanning tunneling microscopy to image the Kondo resonance in a nonconventional Kondo lattice formed by self-assembled oxygen (O_2) molecules, which are paramagnetic, on the gold reconstructed surface [Au(110)-1×2]. The interplay between the intermolecular coupling for molecules adsorbed along chains and the onsite Kondo effect leads to the coexistence of both local and nonlocal Kondo screening at the atomic level. The latter provides evidence for collective deconfinement of magnetization induced in Au, whereas the former shows local "hybridization" between the Kondo clouds of nearest-neighbor O_2 molecules.

The Kondo effect arises from spin-flip scattering processes of itinerant electrons around localized spins of magnetic impurities (*1*–*5*). When individual local spins are brought into a spatially ordered lattice, remarkably rich many-body behaviors of the Kondo systems can appear and require an understanding of how the intersite coupling affects the Kondo screening (*6*–*9*). Below a characteristic temperature T^*, a collective local-moment deconfinement develops and leads to nonlocal Kondo screening (*10*, *11*). The coherence temperature T^* defines an energy scale different from the single-impurity Kondo temperature T_K (*12*, *13*) and is believed to be controlled by the nearest-neighbor intersite coupling (*11*, *14*). There is no cohesive understanding for the Kondo lattice systems due to the complex interplay between single-site Kondo screening and intersite coupling, but this interplay can be enhanced in systems with reduced spatial dimensions through quantum confinement effects (*15*, *16*).

Here, we illustrate the intersite coupling effect in a two-dimensional (2D) Kondo lattice formed

[1]Department of Physics and Astronomy, University of California, Irvine, CA 92697–4575, USA. [2]International Center for Quantum Materials, Peking University, Beijing, P.R. China 100871. [3]Department of Physics, Xiangtan University, Hunan, P. R. China 411105. [4]Department of Chemistry, University of California, Irvine, CA 92697–4575, USA.

*To whom correspondence should be addressed. E-mail: wilsonho@uci.edu

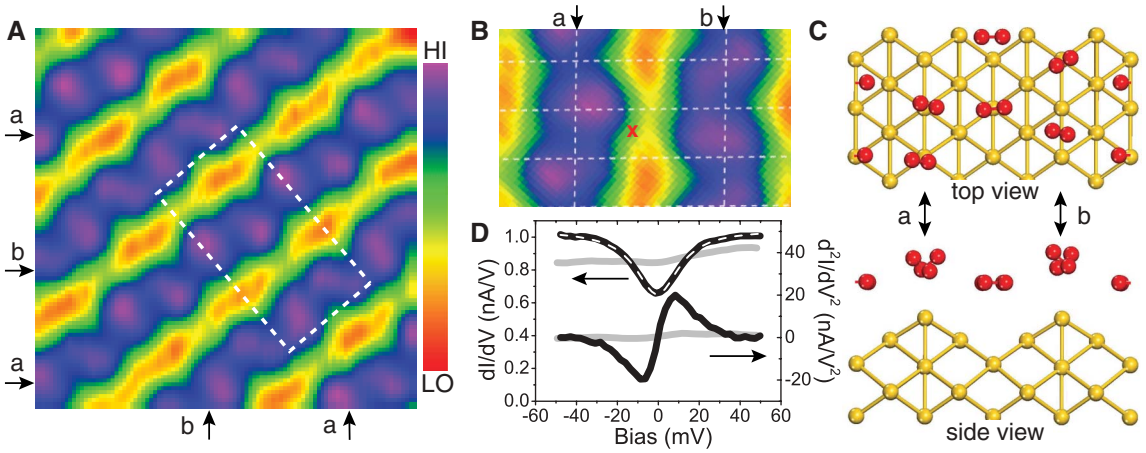

Fig. 1. (**A**) Constant-current STM topography of the O_2 monolayer (34 × 34 Å^2). The 3×4 unit cell is highlighted by a dashed rectangle. The two different kinds of O_2 chains, a and b, are distinguishable. (**B**) Zoom-in image (10 × 17 Å^2) of chains a and b with Au(110)-1×2 lattice superimposed to show the adsorption sites of the O_2 molecules. All the STM topographic images were acquired with V = 0.5 V, I = 0.1 nA. (**C**) DFT calculations for the configuration of the O_2 monolayer corresponding to the area in (B). Oxygen and gold atoms are denoted by red and golden spheres, respectively. (**D**) dI/dV and d^2I/dV^2 spectra taken on (at point marked × in B, black curves) and off (gray curves) the O_2 monolayer. Set point: V = 0.1 V and I = 0.1 nA. The dashed white curve shows a fit to the dI/dV with the Fano equation described in the text.

by a self-assembled monolayer of oxygen molecules on the Au(110)-1×2 reconstructed surface at 10 K (*17*). The weak interaction between O_2 and gold preserves the magnetic ground state of gas-phase O_2 molecules and leads to a Kondo resonance around the Fermi energy (*2*). We visualized the interplay between the onsite Kondo screening and intersite coupling with a scanning tunneling microscope (STM) and achieved high spatial resolution by using the Kondo resonance as a local probe (*18*). The observation of delocalized Kondo screening over the entire surface and the intermolecular distance–dependent coherence temperatures in different O_2 lattices provide evidence for the intersite coupling in the O_2 lattice. In addition, the Kondo resonance exhibits periodic enhancements in regions between O_2 molecules analogous to the hybridization between atomic orbitals.

The O_2 molecules at low coverage were highly mobile along the rows of Au(110)-1×2 surface even at 10 K (fig. S1A); some O_2 molecules were occasionally trapped in single-atom defects. With increasing coverage, O_2 molecules formed monolayer islands (fig. S1B) and eventually a complete O_2 monolayer (fig. S1C). The well-ordered O_2 monolayer consists of two different O_2 chains, both on the rows of the Au(110)-1×2 surface (marked as a and b in Fig. 1A). Chain a is composed of O_2 molecules that pair with each other as dimers, whereas chain b shows a pronounced "zig-zag" feature. It is striking that chains a and b alternate, which results in a 3×4 supercell. With the underlying Au(110)-1×2 lattice superimposed, the adsorption sites of O_2 molecules were determined (Fig. 1B). Both O_2 molecules in chain a are bonded nearly on top of gold atoms, whereas in chain b, one O_2 is bonded nearly on top of a gold atom but the other one is adsorbed in the nearby bridge site.

The adsorption configurations were confirmed by ab initio calculations based on the spin-polarized density functional theory (SP-DFT) at the level of generalized gradient approximation (Fig. 1C).

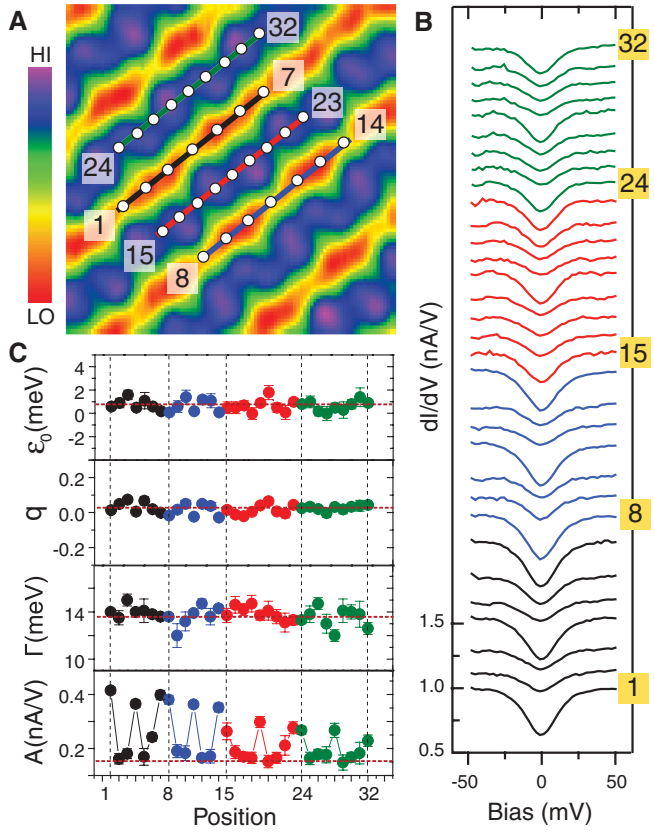

Fig. 2. (**A**) STM topography of an O_2 monolayer, in which the positions of the tip for recording dI/dV spectra in (**B**) are depicted. Set point: 0.1 V and 0.1 nA. Each dI/dV spectrum in (B) is fitted with the Fano equation. (**C**) Spatial dependence of the energetic position ε_0, Fano parameter q, half-width at half-minimum Γ, and the magnitude A of the Kondo resonance at different positions shown in (A). The horizontal dotted lines in the upper three panels of (C) denote the average values: $\varepsilon_0 = 0.7 \pm 0.5$ meV, $q = 0.021 \pm 0.027$, and $\Gamma = 13.7 \pm 0.7$ meV. The horizontal dotted line in the bottom panel of (C) highlights the existence of a uniform background signal level of 0.16 nA/V.

In addition to O_2 chains observed in STM images, we found that additional O_2 molecules were needed in the troughs of the Au(110)-1×2 surface for energy optimization (*17*). These molecules are absent in STM topography because they are about 1.8 Å lower than those on the rows. The O_2 molecules in the top monolayer are weakly bound to the Au(110)-1×2 surface, with an average binding energy of 53 meV/molecule and O-Au bond lengths longer than 2.71 Å. These values correlate well with our experimental observation that the entire monolayer of O_2 molecules desorbed when the STM junction was illuminated by a 532-nm continuous wave laser with power density greater than 15 W/cm^2.

The calculated magnetic moment of each O_2 in the monolayer is 1.997 μ_B, which is near that of the gas phase O_2, 2.0 μ_B in its triplet ground state. The O_2 monolayer forms a ferromagnetic (FM) ground state with a rather weak exchange interaction because the intermolecular distances are as large as 4.2 Å. If we selectively flip the magnetic moment of any O_2 molecule in the lattice, the energy change is less than 1.5 meV, almost within

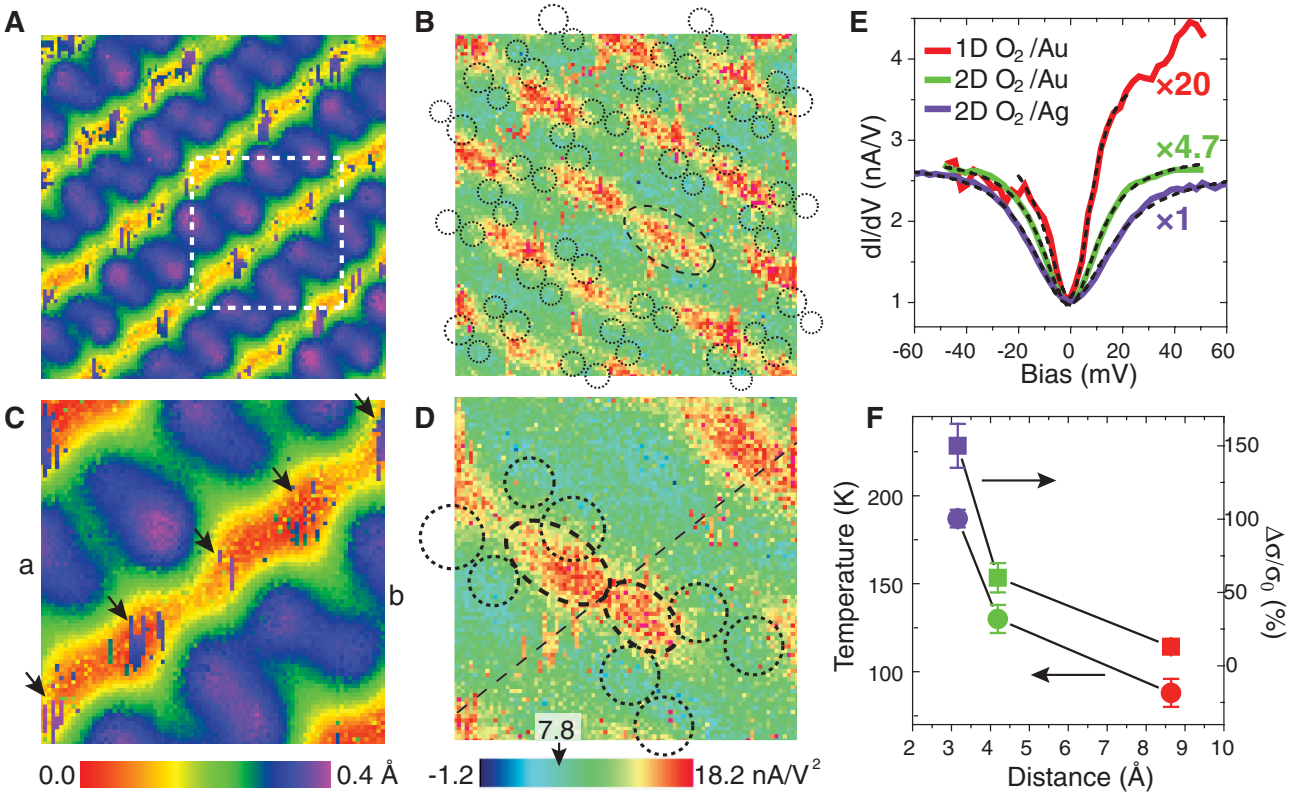

Fig. 3. Topographic images: (**A**) 100×100 pixels, 34×34 Å^2 and (**C**) 85×85 pixels, 14 × 14 Å^2. (**B**) and (**D**) Simultaneously acquired Kondo images by recording the intensity of the positive peak (V = +7 mV) in d^2I/dV^2 spectrum. Set point: V = 0.1 V and I = 0.1 nA. The black arrows in (C) highlight the fuzzy features associated with the weakly bonded O_2 molecules in the trough. The black dashed ellipses in (D) highlight the periodic enhancements. The position of the trough in (C) is denoted by the black dashed line in (D). The big and small circles denote the big and small lobes of each O_2 molecule in chain a, whereas the two circles are similar in size for chain b. (**E**) *dI/dV* spectra of the 2D O_2 lattice on Ag(110) (violet), 2D O_2 lattice on Au(110) (green), and 1D O_2 chain on Au(110) (red). The red and green curves are multiplied by factors of 20 and 4.7, and offset by 14.2 nA/V and 2.1 nA/V, respectively. The dashed black curves show the fits to the data with the Fano equation. (**F**) The coherence temperature and the resonance magnitude (the conductance change $\Delta\sigma$ of the Kondo dip normalized by the zero-bias conductance σ_0) as a function of the intermolecule distance for the three O_2 lattices.

the error range of typical DFT calculations (*17*). Each molecule can flip its magnetic moment almost freely at 10 K, uninhibited by exchange coupling to adjacent molecules. The lack of traditional Ruderman-Kittel-Kasuya-Yoshida interactions makes the O_2 lattice different from heavy fermion materials because the intersite coupling arises from the long-range coherence in the periodic lattice.

A symmetric Lorentzian-like dip was observed around the Fermi level (V = 0) in the *dI/dV* curve, in sharp contrast to the flat spectrum taken over the clean Au surface (Fig. 1D). No other spectroscopic features were observed throughout the bias range from –250 to 250 mV (fig. S1D). The spectroscopic dip has very large magnitude, reaching about 65% of the zero-bias conductance (*17*, *19*). By fitting the *dI/dV* curves with the Fano equation $\frac{dI(V)}{dV} = A\frac{(\varepsilon+q)^2}{1+\varepsilon^2} + B \left[\text{with } \varepsilon = \frac{(eV-\varepsilon_0)}{\Gamma}\right]$, where A is the magnitude, B is the background *dI/dV* signal, q is the Fano parameter, ε_0 is the energetic position, and Γ is the half-width at half-minimum (*20*–*22*), we obtained Γ = 13.5 ± 0.2 meV, which corresponds to a coherence temperature T^* of 130 ± 2 K (*23*). The Fano parameter q obtained in the fit is only about 0.013 ± 0.004, which implies that almost all electrons from the tip tunnel into the conduction states of the Au substrate modified by the Kondo resonance (*22*). If Γ has negligible spatial dependence, as discussed below, it is more accurate and convenient to extract the value of A from the d^2I/dV^2 extrema than from the *dI/dV* amplitude, especially when the Kondo signal is weak (*24*).

The *dI/dV* spectra recorded over the points in Fig. 2A along the rows and troughs on the Au(110)-1×2 surface are displayed in Fig. 2B. The spatial dependences of ε_0, q, and Γ of the Kondo resonance extracted from these curves are negligible (Fig. 2C). Similar spatial invariance of q observed for Co adatoms on the Cu(111) surface was ascribed to the dominance of tunneling into the substrate conduction band (*25*, *26*).

The Kondo magnitude, A, however, exhibits pronounced periodic enhancements along the rows and troughs (Fig. 2C, bottom), with variations up to 0.25 nA/V. Notably, A does not go to zero; its minimum approaches a constant of 0.15 nA/V (dotted line in Fig. 2C, bottom). The larger enhancements for trough positions cannot be simply attributed to the lower tip position. For example, the tip heights at points 2 and 3 are smaller by 0.1 Å than that at point 1, but the signals there are close to the minimum level.

We obtained more comprehensive information on the spatial distribution of the Kondo resonance by constructing Kondo images of the d^2I/dV^2 signals that were simultaneously acquired with the topography (Fig. 3A). The Kondo image of an ordered O_2 lattice (Fig. 3B) was obtained by fixing the bias at the positive peak position (7 mV) in the d^2I/dV^2 spectra. The image obtained at the negative dip (–7 mV) is basically the same, except for the change in sign. The Kondo image shows a delocalized uniform background signal (7.8 nA/V^2, equivalent to 0.16 nA/V in *dI/dV*) superimposed with a periodic enhancement of localized Kondo signal (up to 18.2 nA/V^2, equivalent to 0.38 nA/V in *dI/dV*), in agreement with the mapping data in Fig. 2C. The same (3×4) periodicity in Fig. 3, A and B, implies that the Kondo signal is intimately correlated with the geometric structure of the O_2 monolayer.

The localized enhancements in the Kondo image are characterized by a series of elliptical lobes, one of which is highlighted in Fig. 3B (dotted ellipse). These lobes form in pairs and are elongated along the direction nearly perpendicular to the rows of the underlying Au(110) lattice. A more accurate description of the lobes, however, requires Kondo imaging with finer

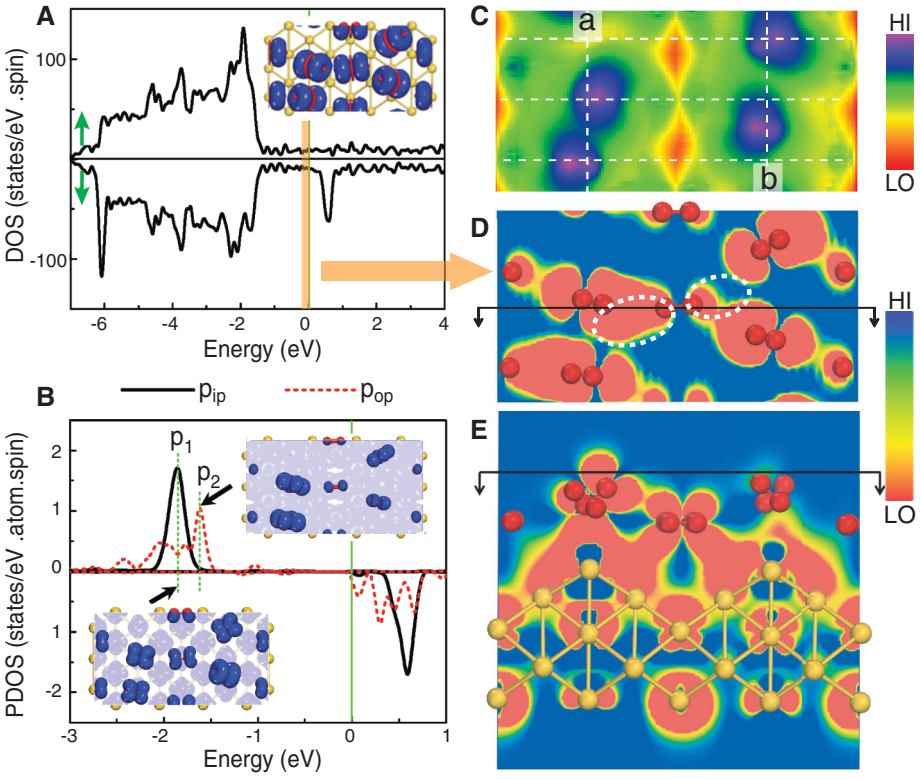

Fig. 4. (**A**) Total density of states. (Inset) Isosurfaces of total spin density of O_2/Au(110). (**B**) Projected density of states at Γ point in O_2 molecules of chain a. (Insets) Isosurfaces of energy-sliced charge densities for states within ±0.05 eV around two peaks pointed out by arrows; p_{ip} and p_{op} represent the projected DOS of in-plane and out-of-plane orbitals, respectively. Positive and negative values indicate states in the majority and minority spin channels, respectively. Fermi level is at 0. (**C**) Simulated STM topography based on the Tersoff and Hamann tunneling model, 3 Å above the topmost oxygen atom for states between 0 and 0.5 eV. (**D** and **E**) The top and side views, respectively, of the spin density for states within −0.25 eV to E_f [beige vertical bar in (A)]. The red color in (D) and (E) represents negative spin densities. The positions of the horizontal plane in (D) and the vertical plane in (E) are highlighted by the black lines in (E) and (D), respectively. The white dotted ellipses in (D) represent the lobes of Kondo enhancement highlighted as black dashed ellipses in Fig. 3D.

spatial resolution (Fig. 3, C and D). The lobe within the dashed ellipse in Fig. 3B could be resolved into two smaller lobes separated by the trough of the Au(110)-1×2 surface (highlighted by two black dashed ellipses in Fig. 3D). Periodic, fuzzy features appeared in the trough (indicated by the arrows in Fig. 3C) when the tip was brought close to the surface such that the tunneling gap was below that set by 0.2V/0.1nA. We attribute the fuzzy regions to O_2 molecules in the trough (Fig. 1C).

Four main features were extracted from Fig. 3, B and D: (i) In both chains a and b, the Kondo enhancements were mainly localized at the ends of O_2, but displaced from the molecular axis. (ii) For chain b, the Kondo enhancement was in the middle between two adjacent O_2 molecules. (iii) For chain a, the Kondo enhancement was next to the "big circle" of the O_2 molecules and aligned with the enhancement in chain b. (iv) The Kondo enhancements arising from chains a and b were correlated with each other to form a linear repeating unit of four lobes (Fig. 3, B and D).

The delocalization of the Kondo signal arises from the collective deconfinement of magnetization in the Kondo lattice below the coherence temperature T^* (*6*, *10*, *11*). The development of the nonlocal Kondo screening is attributed to the intersite coupling (*14*). In addition, as shown in Fig. 3, E and F, the measured coherence temperature T^* (130 K) of the O_2 lattice, with intermolecular distance of 4.19 Å, lies in between that of 1D O_2 chain on Au(110) (88 K) with a larger intermolecular distance (8.64 Å) and that of 2D O_2 lattice on Ag(110) (187 K) with a smaller intermolecular distance (3.16 Å) (*17*). The coherence temperature of the O_2 lattice is thus enhanced with decreasing intermolecular distance.

Localization of the Kondo enhancement signal at the ends of molecules implies that the $2\pi^*$ antibonding states of O_2 are responsible. The calculated isosurfaces of spin density in the inset in Fig. 4A indicate that the magnetization mainly stems from $2\pi^*$ orbitals of the triplet O_2 (*27*). Curves of the total density of states (DOS) in Fig. 4A show that the Au *d* band is well below the Fermi level and that states around E_F are free-electron like. The $2\pi^*$ orbitals of O_2 have an exchange splitting of 2.5 eV, as indicated by the local density of states in Fig. 4B, for O_2 molecules in chain a. The crystal field of Au(110) causes the in-plane (p_{ip}) and out-of-plane (p_{op}) orbitals of O_2 to be split and broadened into resonances. The calculated topographic image in Fig. 4C reproduces the main features of the experimental data in Fig. 1B.

The Kondo effect depends on the responses of itinerant electrons, so it is instructive to analyze the spin density near the Fermi level from states within a range of −0.25 eV to E_f, in both horizontal and vertical planes (Fig. 4, D and E). This spin density is mostly negative (antiparallel to the local magnetization of O_2), a common ground-state feature of the Kondo liquid. The induced spin polarization in Au is rather delocalized (Fig. 4E), in good accordance to the uniform background Kondo signal shown in Fig. 3, B and D.

The experimental image of the Kondo enhancement could be related to the DFT spin density of free-electron states around the Fermi level. The Kondo signal is mostly strong at locations where O_2-induced spin clouds start to overlap, as highlighted by white ellipses in Fig. 4D. The Kondo enhancements shift away from the O sites as a result of the coupling between single-site Kondo screening, which is analogous to orbital hybridization: The "bonding" between Kondo clouds of adjacent O_2 molecules results in the Kondo signal enhancements between them. In a disordered O_2 lattice, the Kondo enhancement is very sensitive to the intermolecular distance (*17*). The Kondo magnitude is always enhanced where the neighboring O_2 molecules are closer and their "Kondo bond" gets stronger (Fig. 3F and fig. S6C). The O_2 molecules in troughs are important in bridging the "Kondo bonds" across chains a and b for the generation of the spatial pattern of the Kondo enhancement in Fig. 3, B and D. Therefore, the Kondo screening in the O_2 lattice is collective, and the Kondo moments bind when they are near each other.

During the Kondo scattering process, itinerant electrons flip their spins by interacting with either the p_{ip} or p_{op} state of O_2, such that the *z* component of the O_2 spin (S_z) is switched between 0 and ±1 without energy cost because the magnetic anisotropy energy is negligible (*17*). Given that there is only one screening channel available in our experimental geometry (the conduction states from the Au substrate), only one electron spin of O_2 can be flipped at a time, such that the O_2 spins are only partially screened. The O_2 lattice resembles an "underscreened Kondo-lattice," as discussed for a spin-1 Kondo model (*28*–*30*) and provides an ideal test ground for studying the competition between the Kondo effect, orbital ordering, and long-range spin coherence.

References and Notes

1. J. Kondo, *Prog. Theor. Phys.* **32**, 37 (1964).
2. A. C. Hewson, *The Kondo Problem to Heavy Fermions* (Cambridge Univ. Press, Cambridge, 1993).
3. V. Madhavan V, W. Chen, T. Jamneala, M. F. Crommie, N. S. Wingreen, *Science* **280**, 567 (1998).
4. D. Goldhaber-Gordon *et al.*, *Nature* **391**, 156 (1998).
5. S. M. Cronenwett, T. H. Oosterkamp, L. P. Kouwenhoven, *Science* **281**, 540 (1998).

6. H. von Löhneysen, A. Rosch, M. Vojta, P. Wölfle, *Rev. Mod. Phys.* **79**, 1015 (2007).
7. P. Aynajian *et al.*, *Proc. Natl. Acad. Sci. U.S.A.* **107**, 10383 (2010).
8. A. R. Schmidt *et al.*, *Nature* **465**, 570 (2010).
9. P. Wölfle, Y. Dubi, A. V. Balatsky, *Phys. Rev. Lett.* **105**, 246401 (2010).
10. S. Nakatsuji, D. Pines, Z. Fisk, *Phys. Rev. Lett.* **92**, 016401 (2004).
11. Y. F. Yang, Z. Fisk, H. O. Lee, J. D. Thompson, D. Pines, *Nature* **454**, 611 (2008).
12. Th. Pruschke, R. Bulla, M. Jarrell, *Phys. Rev. B* **61**, 12799 (2000).
13. S. Burdin, A. Georges, D. R. Grempel, *Phys. Rev. Lett.* **85**, 1048 (2000).
14. S. Nakatsuji *et al.*, *Phys. Rev. Lett.* **89**, 106402 (2002).
15. T. T. Ong, B. A. Jones, *Phys. Rev. Lett.* **103**, 066405 (2009).
16. H. Shishido *et al.*, *Science* **327**, 980 (2010).
17. Materials and methods are available as supporting material on *Science* Online.
18. P. Wahl *et al.*, *Phys. Rev. Lett.* **98**, 056601 (2007).
19. For the 2D O_2 lattice formed on Ag(110) with a smaller intermolecular distance, the resonance magnitude can even exceed 100% of the zero-bias conductance (Fig. 3E).
20. U. Fano, *Phys. Rev.* **124**, 1866 (1961).
21. M. Plihal, J. W. Gadzuk, *Phys. Rev. B* **63**, 085404 (2001).
22. M. Ternes, A. J. Heinrich, W. D. Schneider, *J. Phys. Condens. Matter* **21**, 053001 (2009).
23. The intrinsic coherence temperature T^* was deconvoluted from the measured Kondo width Γ by subtracting the contributions from the tip temperature (T_{tip}), sample temperature (T_{sample}), and the bias modulation (V_{ac}): $2\Gamma = \sqrt{(3.2k_BT_{tip})^2 + (5.4k_BT_{sample})^2 + (2\sqrt{2}V_{ac})^2 + (2k_BT^*)^2}$.
24. B. C. Stipe, M. A. Rezaei, W. Ho, *Science* **280**, 1732 (1998).
25. N. Knorr, M. A. Schneider, L. Diekhöner, P. Wahl, K. Kern, *Phys. Rev. Lett.* **88**, 096804 (2002).
26. C. Y. Lin, A. H. Castro Neto, B. A. Jones, *Phys. Rev. Lett.* **97**, 156102 (2006).
27. L. Pauling, *The Nature of the Chemical Bond* (Cornell University Press, Ithaca, NY, 1960).
28. P. Schlottmann, P. D. Sacramento, *Adv. Phys.* **42**, 641 (1993).
29. B. Coqblin, M. D. Núñez-Regueiro, A. Theumann, J. R. Iglesias, S. G. Magalhães, *Philos. Mag.* **86**, 2567 (2006).
30. J. J. Parks *et al.*, *Science* **328**, 1370 (2010).

Acknowledgments: Supported by the National Science Foundation under grant DMR-0606520 (W.H.) and the Department of Energy under grant DE-FG02-05ER46237 (R.W.). Y. J. acknowledges support by the 985 Program of Peking University and the National Science Foundation of China. DFT calculations were performed on supercomputers at the National Energy Research Scientific Computing Center. We thank D. L. Mills, J. M. Lawrence, and W. Ji for enlightening discussions. The authors declare no competing financial interests.

Supporting Online Material

www.sciencemag.org/cgi/content/full/333/6040/324/DC1
Materials and Methods
SOM Text
Figs. S1 to S7
Table S1
References

18 March 2011; accepted 24 May 2011
10.1126/science.1205785

Directing Zeolite Structures into Hierarchically Nanoporous Architectures

Kyungsu Na,[1,2] Changbum Jo,[1,2] Jeongnam Kim,[1] Kanghee Cho,[1,2] Jinhwan Jung,[1,2] Yongbeom Seo,[1,2] Robert J. Messinger,[3] Bradley F. Chmelka,[3] Ryong Ryoo[1,2]*

Crystalline mesoporous molecular sieves have long been sought as solid acid catalysts for organic reactions involving large molecules. We synthesized a series of mesoporous molecular sieves that possess crystalline microporous walls with zeolitelike frameworks, extending the application of zeolites to the mesoporous range of 2 to 50 nanometers. Hexagonally ordered or disordered mesopores are generated by surfactant aggregates, whereas multiple cationic moieties in the surfactant head groups direct the crystallization of microporous aluminosilicate frameworks. The wall thicknesses, framework topologies, and mesopore sizes can be controlled with different surfactants. The molecular sieves are highly active as catalysts for various acid-catalyzed reactions of bulky molecular substrates, compared with conventional zeolites and ordered mesoporous amorphous materials.

Nanoporous materials possessing pores of molecular dimensions can be used to separate or selectively adsorb guest molecules according to size and shape (*1*–*3*). Zeolites are the best-known group of these molecular sieves, constituting a family of crystalline microporous aluminosilicate minerals (~200 structures) (*1*, *4*). The pore diameters, shapes, and connectivities are specified according to their framework structures, which typically have pore diameters <2 nm. Zeolites are also acid catalysts, cation-exchange materials, and nanoparticle supports, and they exhibit high thermal, hydrothermal, and mechanical stabilities (*4*–*6*). The framework acidity may be tailored by the substitution of different heteroatoms (for instance, aluminum) into the framework. Thus, zeolites have diverse applications and occupy >40% of the entire solid catalysts currently used in the chemical industry (*6*). Nevertheless, zeolite applications are limited to small molecules that can diffuse through the narrow microporous frameworks.

The microporosity of zeolites is generated by the incorporation of pore-generating species such as alkyl-ammonium molecules, which compensate negative charges on the crystallizing silicate framework (*4*, *7*). Such "porogens" can be removed (e.g., by thermal calcination), generating a microporous framework. Several porogens can aggregate to generate pores that are larger than those produced by nonaggregating porogens, but thus far resulting crystalline zeolite structures have been limited to pore diameters <2.2 nm (*8*). In 1992, Kresge *et al.* reported a supramolecular templating mechanism that used surfactant aggregates as porogens to synthesize ordered mesoporous materials [e.g., Mobil Composition of Matter No. 41 (MCM-41)] (*9*). The discovery of this supramolecular porogenic mechanism extended the application of molecular sieves to the mesoporous range (2 to 50 nm). Initially, these mesoporous molecular sieves (MMSs) attracted attention as large-pore acid catalysts for various reactions involving bulky molecules (*3*, *9*, *10*). However, due to their noncrystalline frameworks, these MMSs exhibited insufficient framework acidities and, consequently, low catalytic activities (*3*). Tremendous efforts were made in recent years to synthesize ordered MMSs with crystalline frameworks (*11*–*19*). However, such ordered MMSs were difficult to obtain, except for the use of three-dimensionally ordered mesoporous carbon as a template (*17*). A di-quaternary ammonium surfactant was recently tested as a porogen for such MMSs, but the synthesis yielded two-dimensional (2D) MFI zeolite nanosheets (*18*, *19*).

We present a family of MMSs in which the mesopore walls are zeolitelike microporous crystalline aluminosilicate frameworks. The syntheses were performed with a series of gemini-type, polyquaternary ammonium surfactants that could generate micropores and mesopores simultaneously (fig. S1 and table S1) (*20*). Hexagonal mesostructures were generated by aggregation of the surfactant molecules, whereas the crystallization of microporous frameworks was directed by quaternary ammonium groups within the mesopore walls. One notable member of this dual-porogenic surfactant family has a molecular formula of $C_{18}H_{37}$–$N^+(CH_3)_2$–C_6H_{12}–$N^+(CH_3)_2$–C_6H_{12}–$N^+(CH_3)_2$–$C_{18}H_{37}(Br^-)_3$ (abbreviated as 18–N_3–18) (Fig. 1A). This surfactant has a zeolite-directing head group composed of three quaternary ammoniums connected with –C_6H_{12}– alkyl spacers and two hydrophobic –$C_{18}H_{37}$ alkyl tails. Hydrothermal synthesis using this surfactant resulted in a hexagonally ordered MMS with 1.7-nm-thick crystalline MFI-like microporous frameworks (Fig. 1 and figs. S2 and S3). The use of surfactants with different head groups, which include higher numbers of quaternary ammonium groups and the presence of phenyl rings, resulted in MMSs with thicker mesopore walls and different zeolitelike frameworks (Table 1 and figs. S4 to S10). Although the extent of mesostructural order decreases as the wall thickness increases, the thickness of the crystalline walls was uniform

[1]Center for Functional Nanomaterials, Department of Chemistry, KAIST, Daejeon 305-701, Korea. [2]Graduate School of Nanoscience and Technology (WCU), KAIST, Daejeon 305-701, Korea. [3]Department of Chemical Engineering, University of California Santa Barbara (UCSB), Santa Barbara, CA 93106–5080, USA.

*To whom correspondence should be addressed. E-mail: rryoo@kaist.ac.kr